Energy Conversion and Management 347 (2026) 120532

Contents lists available at ScienceDirect

Energy Conversion and Management

journal homepage: www.elsevier.com/locate/enconman

Research Paper

High energy density long-term thermochemical energy storage composite based on salt and wood-derived activated biochar

Ali Kasebi Vayghan, Maryam Roza Yazdani McCord *, Annukka Santasalo-Aarnio, Ari Seppälä

Aalto University School of Engineering, Department of Energy and Mechanical Engineering, Energy Conversion and Systems, P.O. Box 14400, FI-00076 Aalto, Finland

ARTICLE INFO

Keywords:
Thermochemical energy storage
Sorption
Hygroscopic salts
Biochar
$CaCl_2$

ABSTRACT

Hygroscopic salts as thermochemical energy storage materials stand out for their substantial energy storage density and long-term storage capability, but challenges like agglomeration, deliquescence, and mass transfer issues during sorption hinder their practical application. To resolve these problems, a nature-inspired, sustainable, and inexpensive composite composed of a wood-derived porous activated biochar matrix and $CaCl_2$ as active component is developed through an impregnation method. This study investigates how matrix particle size affects the energy storage density and cyclic stability of the composite. In addition, this research analyzes the salt leakage and evaluates the stability of the composite by using an accurate quantitative method. A simultaneous thermal analyzer coupled with a humidifier was used to analyze the energy storage density. Scanning electron microscopy and X-ray micro-computed tomography were used to analyze salt deposition on the outer surface and inner porous structure of the matrices. The surface area and porosity of the matrix and composite samples were characterized by analyzing nitrogen adsorption/desorption isotherms. Derived from cellular and vascular channels of wood, the activated biochar matrix shows a multi-scale porous structure that not only has exceptional surface area but also facilitates mass transfer as well as successful salt impregnation. A particle diameter between 354 to 595 μm leads to synthesis of the composite with optimal performance, exhibiting an initial energy storage density of approximately 2480 J/g. The energy storage density of this composite remains stable at 2310 J/g and 1780 J/g after 10 consecutive hydration/dehydration and 5 leakage test cycles respectively.

1. Introduction

Energy is vital for modern economy and society in numerous global challenges related to e.g. the environment, security, and geopolitics. Since fossil fuels are non-renewable and over 75 % of global carbon dioxide emissions originates from them, it is essential to find alternative sustainable solutions. While the share of renewable energy in power generation is steadily increasing, fossil fuels continue to dominate, primarily due to the intermittency of renewables and the high capital costs associated with their deployment [1]. For instance, technologies like solar thermal collectors can only function during the day when solar energy is available. By coupling solar thermal collectors with a thermal energy storage (TES) system, surplus daytime heat can be retained and utilized later, when solar heat is not accessible. Similarly, seasonal thermal energy storage involves storing thermal energy during periods of surplus for later use, but unlike short-term storage, the energy can be retained for months rather than just a few hours [2]. Alternately, industrial waste heat can be recovered and used as the heat source to charge a TES system [3].

Thermal energy storages can be classified into three different groups: sensible heat storage (SHS), latent heat storage (LHS), and thermochemical energy storage (TCES) [2,4–6]. In SHS, which is the most traditional form of TES, thermal energy is stored by elevating the temperature of a heat storage material without any phase transition. For example, water [7], molten salts [8], or even rocks [9] can be used as SHS mediums. LHS operates based on the phase transition of an energy storage material. LHS materials can originate from organic (e.g., paraffins, esters, fatty acids, alcohols, and polymers), inorganic (e.g., metals and salts), or combination of them [10,11]. Compared to SHS systems, LHS systems provide higher energy storage density within a smaller temperature range [12]. In TCES, energy is stored and released through a repeatable chemical reaction [13]. TCES materials generally have

* Corresponding author.
E-mail address: roza.yazdani@aalto.fi (M.R. Yazdani McCord).

https://doi.org/10.1016/j.enconman.2025.120532
Received 21 July 2025; Received in revised form 29 August 2025; Accepted 14 September 2025
Available online 24 September 2025

significantly higher energy density than SHS and LHS materials. Moreover, heat can be stored without loss as long as the reactive chemicals are not in contact with each other [13,14], eliminating the necessity of thermal insulation during storage period [15]. TCES materials can be used across a broader temperature range and offer more flexibility in controlling the output temperature compared to LHS materials [14].

Sorption-based TCES is a term used to describe a specific type of TCES. In sorption-based TCES, an absorbate substance is absorbed by the absorbent material in an exothermic process, (discharging), and the product can be dried again in an endothermic process (charging) [16]. Compared to TCES materials that work without sorption, sorption-based TCES typically exhibits weaker energy bonds between the reactants, allowing it to operate at lower temperatures [6]. Their operating temperature range makes them well-suited for applications such as space and water heating, and they can be charged using renewable sources like solar energy or recovered industrial waste heat [17,18].

Hygroscopic salts, including their hydrated forms, are promising sorption-based TCES materials due to their high storage energy density, moderate working temperature, and affordability [16]. The general reaction of these salts with water vapor is described as follows [19]:

$$MX{\cdot}nH_2O(s) + yH_2O(g) \rightleftharpoons MX{\cdot}(n+y)H_2O(s) + y\Delta H_r \quad (1)$$

where ΔH_r represents the enthalpy of the reaction and $MX{\cdot}nH_2O$ and $MX{\cdot}(n+y)H_2O$ are salt hydrates composed of the MX salt with n and n +y moles of H_2O, respectively.

Several factors must be considered when selecting a hygroscopic salt for thermal energy storage, including specific heat, reaction enthalpy, density, sorption/desorption temperature, melting temperature, volumetric changes, reaction kinetics, thermal conductivity, toxicity, environmental safety, cost, and availability [16]. Various salts such as LiCl, LiBr, $LiNO_3$, $Ca(NO_3)_2$, $SrBr_2$, $CaCl_2$, $MgSO_4$, Na_2S, $MgCl_2$, $SrCl_2$, $Al_2(SO_4)_3$, $CaBr_2$, K_2CO_3, KOH, $LaCl_3$, $La(NO_3)_3$, $Na_2S_2O_3$, and $Zn(NO_3)_2$ have potential for use as sorption-based TCES salts, each with its own advantages and disadvantages. Among these, $CaCl_2$ is one of the least expensive options and offers high energy storage density [20,21]. It is widely available, has a low environmental impact, and is produced as a by-product in industries such as soda ash production [22]. The target application of this research is heating of spaces, such as residential buildings. $CaCl_2$ can be used to harvest solar energy and provide a temperature range suitable for this purpose [23], making it the preferred sorbent salt for this study.

Despite the advantages of hygroscopic salts, their performance degrades after several hydration/dehydration cycles due to issues such as deliquescence, agglomeration, and swelling, which occur when the relative humidity exceeds the deliquescence threshold [24,25]. To address these challenges, two main approaches have been explored: impregnating the salt into a porous matrix [25–29] or encapsulating the salt within a porous shell [25,30,31]. Impregnation has been the most studied method due to its cost-effectiveness and the ability to control the final properties of the composite by adjusting parameters such as pore size, salt loading, and topology but controlling salt leakage is challenging. In comparison, encapsulation prevents energy losses by enclosing hygroscopic salt in a stable shell, avoiding coalescence and agglomeration. However, the shell must remain permeable for water vapor diffusion, mechanically stable through thermal cycles, and chemically inert under hydration conditions, which adds to complexity and cost of the method [32]. In this research, the impregnation approach was chosen for its advantages meanwhile by investigating the effect of matrix size on energy storage density and salt leakage, we aimed to minimize its shortcomings.

With a careful selection of porous matrices, cycling stability of a TCES composite can be enhanced by preventing agglomeration, while also improving heat and mass transfer through efficient pathways [33]. Several criteria are considered when selecting host matrices, including thermal conductivity [34], mechanical strength, stability under hydration/dehydration conditions, water affinity, sorption capacity, and cost [20]. Potential matrix materials suitable for impregnation approach include zeolite [35], expanded graphite [36], expanded vermiculite [37], silica gel [38], and activated carbon [39]. While porous activated carbon is low cost and has high porosity and stability, it can cause environment concerns if it is derived from non-renewable sources like coal [33]. Activated biochar derived from wooden biowaste is an inexpensive, eminently porous, and sustainable material to substitute activated carbon and other porous carbon-based materials derived from non-renewable resources [40,41]. Wood has a hierarchical porous structure at multiple length scales [42]. This structure consists of interconnected porous channels allowing multiphase transport of ions, liquids and gases. By carbonization and activation of wood, porosity of the structure can be enhanced further, making it an ideal matrix that can uptake salt solution while allowing humid air to flow through the porous structure. Therefore, to the best of our knowledge in this research, for the first time a porous activated biochar matrix was synthesized from alder wooden chips to host $CaCl_2$ and develop a sustainable TCES composite with remarkable energy storage density.

One of the critical challenges in salt-matrix composites is preventing salt leakage [25,43,44]. However, most studies only propose methods to visually observe leakage for qualitative comparison [25,45–49] or evaluate cyclic stability by measuring changes in the energy storage density, water uptake, or both after consecutive hydration/dehydration cycles using a differential scanning calorimeter (DSC), thermogravimetric analyzer (TGA), or simultaneous thermal analyzer (STA, simultaneous TGA/DSC), respectively [30,33,39,50,51]. The former method is imprecise and lacks quantifiable results, while the latter overlooks energy density drop caused by leakage in TES systems. This limitation arises because leaked salt solution remains in the sample holder, artificially contributing to measured energy storage. While in a scaled-up system, leaked salt may agglomerate and obstruct humid airflow, resulting in slower kinetics and insufficient temperature rise. Additionally, in an open TES system, leaked salt can escape the system entirely, decreasing the energy storage density. This paper introduces an accurate method to measure leakage and material stability, addressing these shortcomings.

In this study we synthesized and characterized a sustainable sorption-based TCES composite composed of activated biochar derived from alder wood and $CaCl_2$ as active salt with long-term space heating applications in mind. For this, after morphology and surface area analysis of the matrix and synthesized composite samples, the energy storage density of them were measured during hydration. Also, the effect of matrix size on energy storage density of the composite and its cyclic performance was investigated to optimize matrix particle size as a synthesis factor. Furthermore, salt-leakage, which is the most remarkable challenge of this type of composites, was analyzed using an innovative and accurate method that we designed specifically for this purpose.

2. Methodology/experimental

2.1. Materials

Calcium chloride dihydrate (ACS reagent grade, assay ≥ 99 %, supplied by Merck KGaA) was used in the preparation of the TES composite. Alder wooden chips (supplied by Biltema) of approximate length between 3 to 8 mm, was used as the source for activated biochar synthesis. Deionized water, with a resistivity of 18.2 MΩ·cm at 25 °C, was utilized to dissolve the salt.

2.2. Method

2.2.1. Synthesis

Fig. 1 summarizes the synthesis steps of the TCES activated biochar/$CaCl_2$ composite.

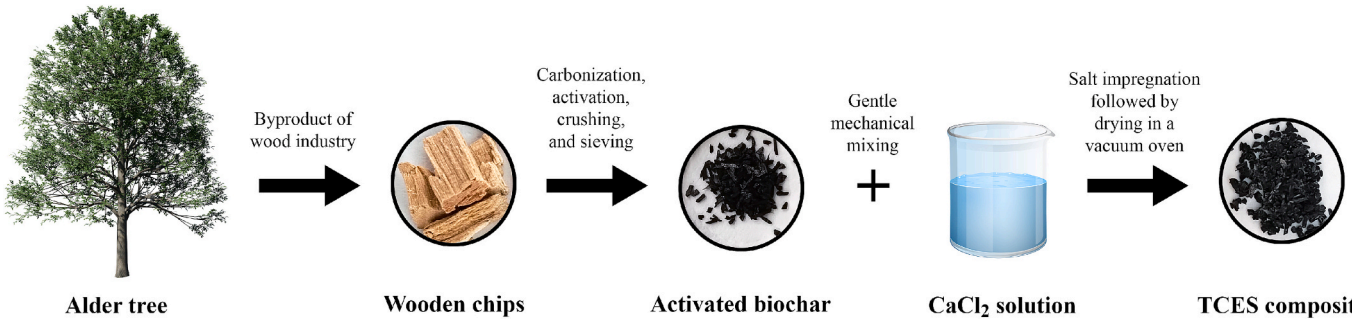

Fig. 1. The summary of synthesis process of the TCES activated biochar/$CaCl_2$ composite.

Wood chips, derived from alder tree, were heated in a furnace to 300 °C at a heating rate of 5 K/min under nitrogen atmosphere and held for one hour to induce carbonization. Following this step, the temperature was further increased to 850 °C at the same heating rate and maintained isothermally for 3 h, during which a humidifier was employed to introduce humidity into the furnace and enhance porosity of the biochar through steam activation [52].

The synthesized activated biochar was gently crushed using a mortar and pestle. The crushed particles were sieved through sieves of different mesh sizes yielding six different size distributions of activated biochar particles, which are listed in the Table 1.

Six sample batches of activated biochar-$CaCl_2$ composite with distinct matrix sizes and a consistent nominal chemical composition of 35 wt% activated biochar and 65 wt% $CaCl_2$ were prepared.

First, a saturated calcium chloride solution with a concentration of 530 g/L was prepared by dissolving an appropriate amount of $CaCl_2{\cdot}2H_2O$ in deionized water, using a magnetic stirrer rotating in a glass beaker. The solution was prepared at its saturation concentration to minimize volume, ensuring just enough liquid to wet the particles and prevent their flotation on the surface of the solution. Then, 0.35 g of activated biochar particles of different particle size distributions were placed in six different glass containers and 1.23 mL of the mentioned solution was added to each container to achieve the desired composition. The mixture in each container was briefly and gently mixed by a spoon to help wetting the activated biochar particles while avoiding damage to the particles. Then the glass containers were sealed with plastic caps, and the samples were let to soak for 4 days in the room conditions. Soaked particles were transferred to another glass container and placed into a vacuum oven to dry out at a vacuum pressure of approximately 0.02 mbar. The samples were heated from room temperature to 100 °C over 3 h. The temperature was then reduced to 80 °C and the samples were dried for an additional 18 h. The resulting dry composite samples were sealed in capped glass containers and stored appropriately for further thermal analysis and characterization. The energy storage performance of the reference $CaCl_2$ sample and the activated biochar matrices with different particle sizes before salt impregnation were also investigated.

Table 1 lists all the samples, their nominal composition, and particle diameter. The particle diameter in this context is determined by the mesh size of the sieves employed.

Table 1
List of the samples, including activated biochar matrices and synthesized composites, their nominal composition, and particle diameter range. The letters B and C in sample name column refer to activated biochar matrices and composite samples respectively. Nominal composition refers to the intended composition of the synthesized samples after drying.

Sample name	Nominal composition		Particle diameter (d) (μm)
	Activated biochar (wt %)	$CaCl_2$ (wt %)	
B1	100	0	$d < 125$
B2	100	0	$125 < d < 250$
B3	100	0	$250 < d < 354$
B4	100	0	$354 < d < 595$
B5	100	0	$595 < d < 1600$
B6	100	0	$1600 < d$
C1	35	65	$d < 125$
C2	35	65	$125 < d < 250$
C3	35	65	$250 < d < 354$
C4	35	65	$354 < d < 595$
C5	35	65	$595 < d < 1600$
C6	35	65	$1600 < d$

2.2.2. Morphology analysis

X-ray micro-computed tomography (micro-CT) has proved to be a potent non-destructive method for analysis of porous micrometer-scaled structure of wood and activated biochar in three dimensions (3D) [53,54]. The sample with the best energy storage performance and its matrix support were analyzed using a Waygate Technologies Phoenix Nanotom® S X-ray microtomography device to obtain morphological insight and analyze salt impregnation in the matrix. The samples were put into a narrow tube and subjected to projections with an exposure time of 3 × 500 ms per projection, covering a full angle of 360° degrees, resulting in 1000 images per sample. The source voltage and current were set at 60 kV and 180 μA respectively. A spacing of 5 mm was maintained between the sample and the source, and 250 mm between the detector and the source. The pixel width, pixel height, and voxel depth were 2 μm.

The brightness and contrast of the images were enhanced using the FIJI software. A single particle of the studied composite sample was isolated and the background was removed. Subsequently, the Volume Viewer plugin within the software was used to generate a 3D model from a stack of 317 images of the isolated particle. The resulting 3D model was animated to visually demonstrate the macroporosity of the structure. It should be noted that finer details, such as thinner cell walls, may be missed in the 3D model due to low contrast with the background and their removal during image processing.

Due to the low contrast between the walls of the activated biochar and empty space in the obtained images of the activated biochar matrix sample, it was not feasible to remove the background. Consequently, this sample was not modeled in 3D.

The morphology of the activated biochar and composite samples were analyzed using a Zeiss Sigma VP field emission scanning electron microscope (FE-SEM). The samples were coated with 5 nm of Au(60 wt %)/Pd(40 wt%) alloy using a Leica EM ACE600 sputter coater to increase electrical conductivity and enhance image quality. Also, the samples were analyzed after hydration to indicate the changes due to leakage. Energy-dispersive X-ray spectroscopy (EDS) mapping of the best sample was performed using an Oxford Instruments Ultim Max 65 detector installed on the same scanning electron microscope (SEM) to examine salt deposition on the outer surface of the matrix. For this purpose, the sample was coated with 8 nm of carbon to enhance the electrical conductivity of the composite and minimize interference in the

EDS spectra.

A Microtrac BELsorp Mini II instrument was used to obtain nitrogen adsorption/desorption isotherms and evaluate surface area and porosity of activated biochar samples B1, B4, B6 and composite samples C1, C4, C6. A combination of Brunauer–Emmett–Teller (BET) [55], Barrett-Joyner-Halenda (BJH) [56], and MP [57] methods were used to estimate the surface area and pore size distribution. To prepare the samples for surface analysis, dry samples were degassed using nitrogen gas at 120 °C for 3 h on a Microtrac BELPrep Vac II Pre-Treatment Station device.

The total surface area of the samples was estimated based on BET surface area calculations. The mesoporous surface area, derived from the BJH method, was subtracted from the BET surface area to estimate the total microporous surface area. The total pore volume was estimated from the absorbed amount of nitrogen at a relative pressure of $P/P_0 = 0.99$. In the context of physisorption, pores can be classified in three groups according to their sizes: macropores with pore widths exceeding 50 nm, mesopores with pore widths between 2 nm and 50 nm, and micropores with pore widths less than 2 nm [58]. It is important to note that the total pore volume calculated from nitrogen adsorption/desorption isotherms doesn't represent the volume of the macropores with diameters larger than 100 nm, as macropores larger than this do not significantly contribute to nitrogen adsorption. To estimate the microporous volume, the mesoporous volume derived from BJH method was subtracted from the estimated total pore volume. Finally, the pore size distribution of the activated biochar matrix samples was plotted using MP method for the pores with diameters up to 2 nm and the BJH method for the pores with diameters between 2 nm and 100 nm.

2.2.3. Thermal energy storage analysis

Thermal energy storage performance of the samples was analyzed using a Netzsch STA 449 F3 Jupiter simultaneous thermal analyzer connected to a ProUmid MHG32 humidifier.

The samples were put into aluminum crucibles. The samples were heated up from 30 °C to 120 °C at a 10 K/min rate and were held at that temperature for 45 min to ensure complete drying. Then they were cooled down to 32 °C at a rate of 3 K/min using a vortex tube cooler and held at that temperature for 15 min. Then the samples were heat up to 35 °C at 0.2 K/min rate and stayed at 35 °C for 15 min to ensure that the temperature is stable. The samples were then hydrated at 35 °C for 3 h using humid nitrogen (99.999 % purity) with a flow rate of 400 mL/min and relative humidity of 35 %. Fig. 2 shows the full cycle of hydration/dehydration steps used to assess the energy storage density of the composite samples. This full cycle was repeated continuously for each sample twice to measure the energy storage density of composite samples and pure $CaCl_2$ and ensure their validity. Each of these measurements were replicated at least twice to ensure repeatability of the experiment.

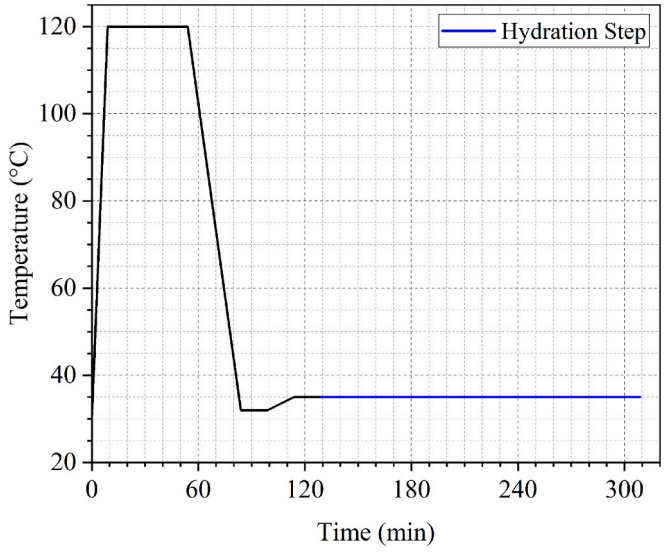

Fig. 2. The full cycle of hydration/dehydration program used to assess the energy storage density of the composite samples.

The energy storage density is calculated by dividing the area enclosed between the DSC curve and a vertical line drawn from the onset of the hydration reaction to the point where it intersects the curve again, by the dry mass of the sample immediately before the hydration step.

As activated biochar samples were found to have negligible water vapor sorption capacity compared to pure salt or composite samples, the hydration time for them was reduced to 1 h and each measurement was replicated once to determine the average energy storage density of the matrices.

The analysis of variance (ANOVA) at 0.05 alpha level was used as the statistical method to indicate if particle size significantly affects the energy storage density of the samples.

The components contributing to the sorption energy density of the composite $\Delta_{sorp}H_C$ (in Joules) are shown in Eq. (2), which modified the equation Barsk et al. [30] used to calculate the reaction enthalpy of pure $CaCl_2$.

$$\Delta_{sorp}H_C = \Delta_r H_{CaCl_2\cdot 6H_2O} + \Delta_m H_{CaCl_2\cdot 6H_2O} + \Delta_{dil}H\left(\xi_{6H_2O}\rightarrow\xi_{eq}\right) + \Delta_{con}H\left(n_{eq}-6\right) + \Delta_{ads}H_B \quad (2)$$

where $\Delta_r H_{CaCl_2\cdot 6H_2O}$ represents the enthalpy of reaction for the hydration of anhydrous calcium chloride to its hexahydrate form; $\Delta_m H_{CaCl_2\cdot 6H_2O}$ denotes the melting enthalpy of $CaCl_2\cdot 6H_2O$; $\Delta_{dil}H\left(\xi_{6H_2O}\rightarrow\xi_{eq}\right)$ corresponds to the dilution enthalpy as the hydration level changes from six water molecules (ξ_{6H_2O}) to the equilibrium level (ξ_{eq}); $\Delta_{con}H(n_{eq}-6)$ refers to the condensation enthalpy of water vapor from the hexahydrate ($n = 6$) to equilibrium state (n_{eq}); and the $\Delta_{ads}H_B$ is the water vapor adsorption enthalpy of the activated biochar.

Assuming the salt is distributed uniformly within the composite, the dry mass of the matrix and the salt content in each sample after impregnation can be approximately estimated from:

$$m_c \times \Delta h_c = m_m \times \Delta h_m + m_s \times \Delta h_s \quad (3)$$

where m_m (g) is the dry matrix mass, Δh_m (J/g) is the specific enthalpy of water vapor adsorption for the matrix, m_s is the mass of salt in the sample, Δh_s is the specific reaction enthalpy of pure salt during hydration, $m_c = m_m + m_s$ is the dry mass of the composite, and Δh_c is the total specific enthalpy of reaction for the composite sample during hydration. Reaction specific enthalpies of Δh_c, Δh_m, Δh_s can be easily obtained based on the STA data. Since part of the porous structure of matrix will be covered by salt after impregnation the adsorption of water vapor into the matrix pores might be limited. Also, because the Δh_m is relatively small compared to the Δh_s, salt content can be estimated easier by using the following equation.

$$\frac{m_s}{m_c} = \frac{\Delta h_c}{\Delta h_s} \quad (4)$$

2.2.4. Cyclic performance analysis

The performance of sorption-based TCES composites can decrease over cycles of hydration/dehydration due to problems such as deliquescence, agglomeration, salt leakage, swelling, and material degradation [59]. Thus, the cyclic performance of the composite samples was evaluated through continuous hydration/dehydration cycling with STA and a leakage test designed in this study.

To evaluate cyclability of the material in STA, samples C2, C3, C4, and pure $CaCl_2$ were selected for testing and subjected to 10 consecutive hydration/dehydration cycles using the setup mentioned earlier and under the same conditions. However, as discussed in the introduction,

this methodology applied in most of published studies, overlooks the effect of salt leakage in energy storage density measurement. The energy storage density was monitored across 10 cycles to evaluate sample degradation apart from leakage over 10 cycles.

Without a true leakage test, the consecutive hydration/dehydration cycling method using a STA is only suitable for assessing material degradation and does not represent their performance and durability in a scaled-up TES system.

For leakage test a custom sample holder was made. First, aluminum foil was cut into a 20 mm diameter disk and shaped into a pan. Then, a smaller filter paper disk was cut and placed at the center, fully covering the bottom of the pan, to absorb any salt that would leak during the hydration/dehydration cycle. The sample holder was put into an oven and heated to 120 °C for 2 h to ensure complete drying. A certain amount of the composite samples was put in the center of the sample holder and was inserted into the STA device. The samples were humidified under the same condition described in the previous section.

After hydration and the absorption of leaked salt by the filter paper, the sample and sample holder were dried again in the oven. The composite samples were then carefully separated from the filter paper and transferred to a glass container. The remaining energy density of the samples were measured by running the same STA program used for the energy storage density measurement on a small amount of the sample after each leakage cycle. The remaining material in the glass container was reserved for the next leakage cycle. The leakage test was performed on samples C1, C2, C3, C4, C5, and C6, with 1, 5, 5, 5, 1, and 1 cycles conducted for each sample, respectively. The reason for conducting more leakage cycles on samples C2, C3, and C4 was their superior energy storage density after the first leakage cycle, which made them the best candidates for further study. One key advantage of estimating leakage based on changes in energy storage density, rather than mass, is that it practically eliminates dependence on the initial amount of composite loaded onto the sample holder or any residual composite particles that may adhere to the holder after hydration.

3. Results and discussion

3.1. Morphology analysis

Here the resulting micro-CT and SEM images as well as EDS maps and nitrogen adsorption/desorption isotherms are analyzed to study the porous structure of the activated biochar matrices and examine salt impregnation in the composite samples.

Fig. 3 presents the micro-CT images of the activated biochar matrix and composite sample. X-ray tomography works based on the penetration of X-ray through materials, revealing their inner structure. Samples with greater thickness and materials with higher X-ray attenuation coefficient appear brighter in the images. Thus, the darker areas in Fig. 3 represent pores and empty spaces between the particles while the brighter areas correspond to the locations of the solid structures. The higher contrast in the composite sample compared to the activated biochar sample is due to the presence of calcium chloride, which has a significantly higher X-ray attenuation coefficient. Fig. 3a exhibits the hierarchical porous structure of sample B4, consisting of two distinct types of macropores with different size ranges. Fig. 3b illustrates uniform $CaCl_2$ deposition on sample C4, coating the pore walls without blocking them. The uniform deposition of salt on the inner walls of the matrix and its penetration to the core are crucial, as salt particles deposited on the outer surface are more susceptible to agglomeration or loss after deliquescence. Also, the open pores of the composite facilitate mass transfer for water vapor during hydration/dehydration process.

Supplementary Video 1 shows an isolated particle of the sample C4 modeled in three dimensions. A series of long vessels stretching from one end to the other end of the particle, allow easy transport of salt solution to the core of the activated biochar. In fact, highly porous tubular structure of wood is designed to transport water upwards by capillary force [60,61]. Also, the cell walls, containing nanoscale pathways, enhance ion transport [61]. These make the well-preserved porous structure of the wood in the activated biochar sample C4 an exceptional salt solution absorbent. Moreover, it can be observed that many vessels and tracheids are not blocked by the salt, expediting water vapor transfer to inner parts of the composite during hydration/dehydration.

Fig. 4a shows the structure of the dried alder wood used to synthesize the activated biochar matrix. In addition to cellulose, hemicellulose, and lignin, which are main compounds of wood structure, wood contains moisture and volatile organic materials [61]. Water as well as existing and formed volatile compounds are removed from the wood pores during pyrolysis and porosity of the resulting carbon-rich activated biochar will be enhanced [62]. Fig. 4b presents sample B6 from the same perspective, showing a more clearly defined structure after decomposition of polymeric compounds and removal of volatiles. Fig. 4c shows sample B4, which preserves the original wood structure while exhibiting increased porosity. In contrast, Fig. 4d demonstrates the unpreserved structure of sample B1 with flaked walls of vessels and tracheids due to excessive crushing of the activated biochar. Fig. 4e and Fig. 4f exhibit the multi-scale hierarchical porous structure of the synthesized activated biochar including vessels, tracheids, and pits, shown by numbers 1, 2, and 3 respectively. The multi-scale pores seen in the SEM images, ranging from 1 μm to almost 50 μm in diameter, facilitate salt solution impregnation and efficient water vapor transport during hydration/dehydration cycles [63].

Fig. 5 includes the images of $CaCl_2$/activated biochar composite

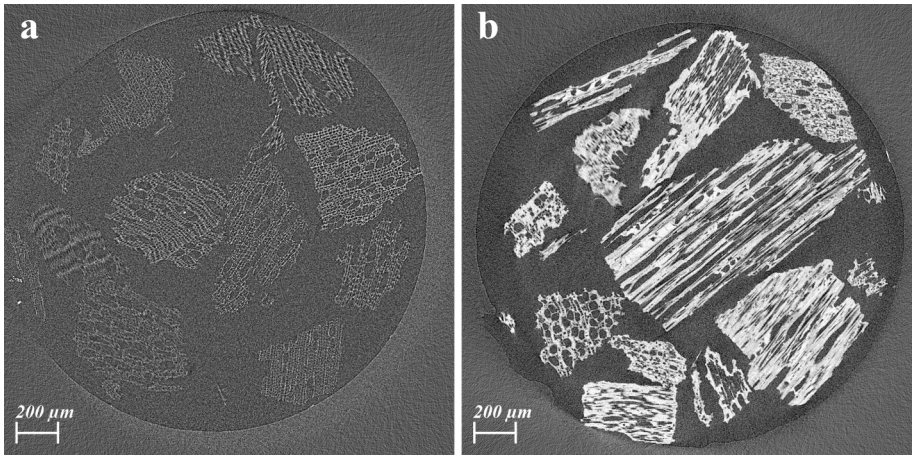

Fig. 3. The micro-CT images of (a) the activated biochar sample B4 (b) the composite sample C4.

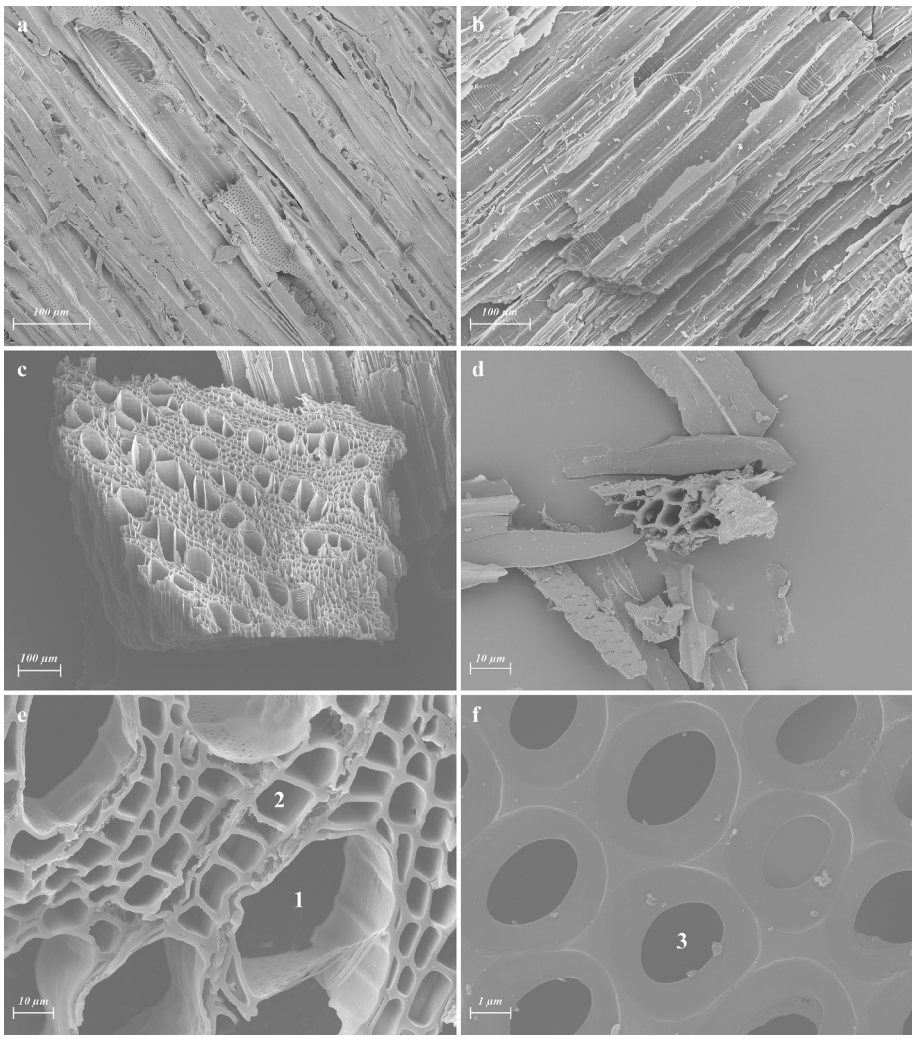

Fig. 4. The SEM image (a) of the alder wood, (b) activated biochar samples B6, (c) B4, (d) B1, (e) B2, and (f) B3 exhibiting a multiscale hierarchical porous structure. Different pore sizes of vessels (1), tracheids (2), and pits (3) on the vessel walls are shown in the picture.

samples. Fig. 5a and 5b illustrate the excessive agglomeration of composite particles in the C1 and C2 samples, respectively. This occurs because smaller particles have a larger surface area relative to their volume. As the surface area covered by the salt increases, more particles are likely to agglomerate. Additionally, decreasing the particle size strengthens the total capillary forces exerted on solution between adjacent particles [64–66]. Capillary force forms bridges of salt solution between the particles and when the solution dries, $CaCl_2$ crystallizes and causes composite particle agglomeration.

Fig. 5c shows reduced agglomeration in sample C3 compared to the smaller particles in samples C1 and C2, consistent with the previously discussed reasons. Fig. 5d1 illustrates further decreased agglomeration and superior salt distribution in C4, without excessive outer surface deposition or pore blockage. Fig. 5d2 magnifies the area outlined by the red rectangle in Fig. 5d1 to better highlight the open pores, which facilitate the flow of salt solution into the matrix. Fig. 5d3 further magnifies the region within the blue rectangle in Fig. 5d2 to show the favorable salt deposition on the inner walls of the activated biochar.

Although agglomeration is not a major concern for large composite particles in samples C5 (Fig. 5e) and C6 (Fig. 5f), excessive salt accumulates on their outer surfaces. This occurs due to a decrease in the total outer surface area of the particles compared to samples with smaller particle sizes, resulting in more salt deposition on the outer surface of each particle. Such deposition is undesirable, as salt on the outer surface is more likely to be removed during the hydration step.

Fig. 6 presents the EDS map of sample C4, illustrating the distribution of elements on the outer surface of a particle. While $CaCl_2$ covers most of the surface area, it preferentially deposits along grooves of tracheids and vessels due to capillary action.

Fig. 7 shows the SEM images of the composite samples after leakage test. Particles in samples C1, C2, and C3 remain agglomerated, with agglomeration decreasing as particle size increases. This is because liquified $CaCl_2$ on the outer surface of the particles can become trapped in gaps between agglomerated activated biochar fragments. Since samples C2 and C3 underwent five leakage cycles, while sample C1 experienced only one, they lost more salt from the outer surfaces of their particles, reducing the severity of agglomeration. After the leakage cycles, the agglomeration issue is not observed anymore in samples C4, C5 and C6. The number of leakage cycles required to detach the agglomerated particles from each other depends on the severity of agglomeration, which increases as particle size decreases. This can be recognized by comparing Fig. 7b, Fig. 7c, and Fig. 7d, which show sample C2, C3, and C4 respectively, all enduring 5 cycles of leakage test. Although some salt deposited on the outer surfaces of their particles has been washed away, the grooves and inner pores retain the salt.

Table 2 shows the surface area and pore volume of the samples B1, B4, B6, C1, C4, and C6. The activated biochar matrix samples exhibit an impressive total surface area and pore volume up to 800 m^2/g and 0.48 cm^3/g respectively. On average, approximately 16 % of the total surface area and 33 % of the total volume of the pores in the activated biochar

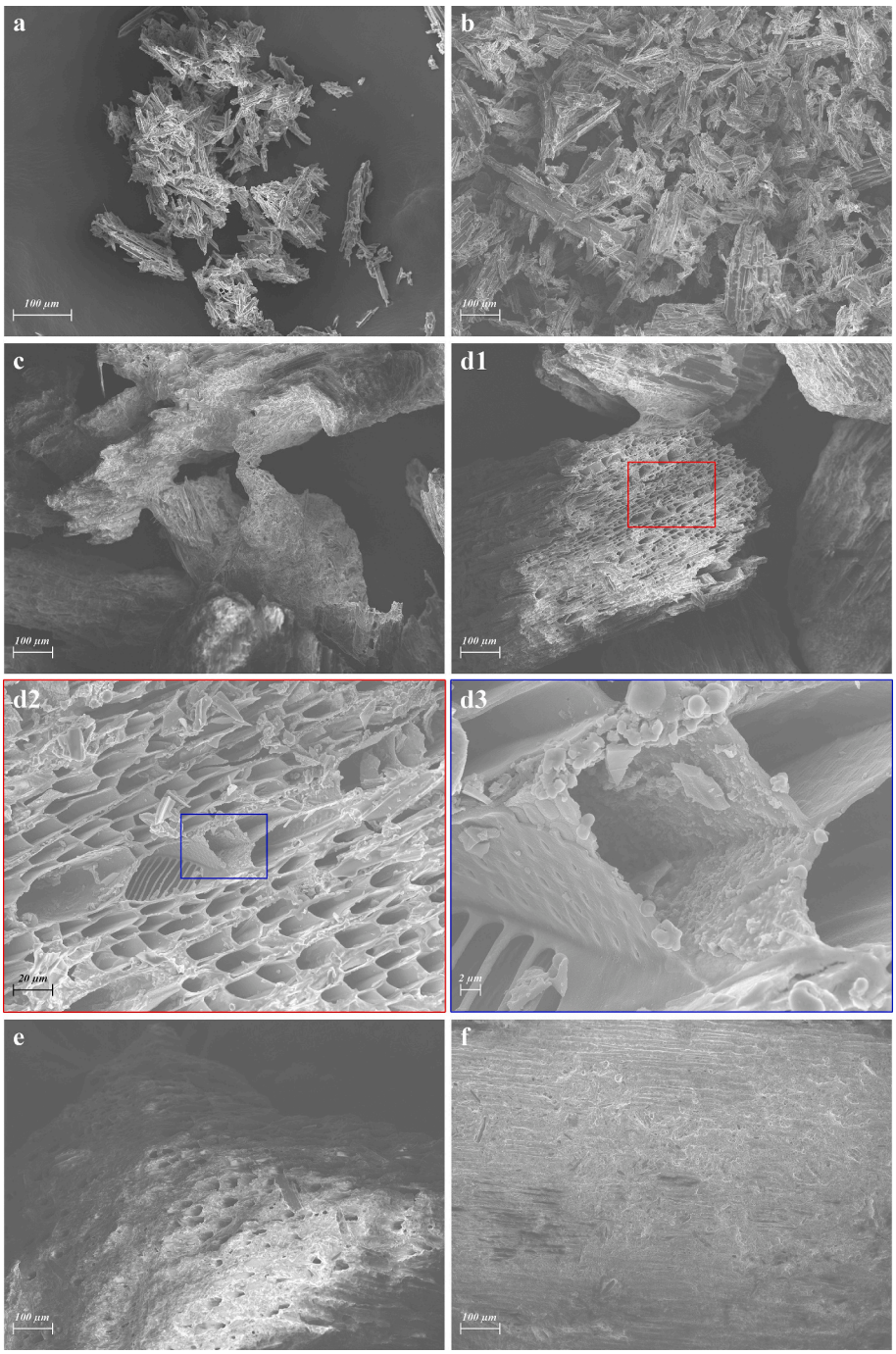

Fig. 5. The SEM image of (a) the synthesized TES composite samples C1, (b) C2, (c) C3, (d1, d2, and d3) C4, (e) C5, and (f) C6 showing activated biochar particles after salt impregnation.

matrix samples originate from their hierarchical mesopores, which significantly enhances mass transfer during hydration/dehydration [67]. Comparison of the B1, B2 and B3 samples shows a slight decrease in total BET surface area with increasing particle size. The total surface area and pore volume of the composite samples, especially the microporous surface area and volume, are significantly lower than those of the activated biochar samples. This indicates effective salt impregnation and highlights the role of micropores in providing substantial surface area to host the salt. The increased relative mesoporous volume (V_{meso}/V_{tot}) and relative mesoporous surface area (S_{meso}/S_{total}) in the composite samples compared to the biochar samples is due to coverage of micropores by the salt while mesopores are less affected by this. Macroporous surface area and volume in activated biochar cannot be measured by nitrogen adsorption, but are visible in Fig. 4c, Fig. 4e, and Fig. 4f. These types of pores are crucial to mass transfer of salt solution during salt impregnation step as well as water vapor mass transfer during hydration/dehydration [61].

Fig. 8a illustrates the nitrogen adsorption/desorption isotherms of the samples B1, B4, B6, C1, C4, and C6. The steep increase in adsorption at low relative pressures in the activated biochar matrices indicates remarkable microporosity. As the relative pressure increases from 0.1 to 0.95, the nitrogen adsorption by activated biochar particles rises approximately linearly without reaching a saturation plateau, indicating the presence of macropores. The nitrogen adsorption/desorption

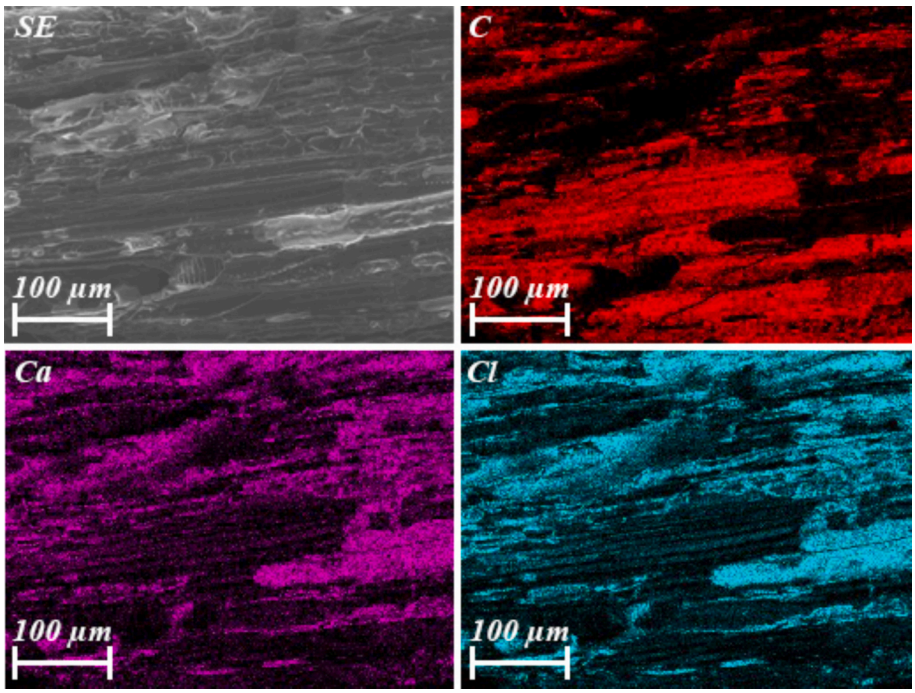

Fig. 6. The EDS map of the activated biochar/$CaCl_2$ composite sample C4 showing the distribution of elements on the outer surface of a single activated biochar particle. SE represents the secondary electron signal, while C, Ca, and Cl indicate the signals corresponding to each element.

isotherms of activated biochar matrices show a hysteresis effect due to capillary condensation in mesopores [68]. In contrast, the adsorption/desorption isotherms of the composite samples show limited overall adsorption, reduced adsorption at low relative pressures, and a negligible hysteresis effect compared to the activated biochar matrix samples, indicating effective salt coverage of microporous and mesoporous surfaces.

Fig. 8b shows the pore size distribution of the matrix samples B1, B4, and B6. The samples exhibit similar pore size distributions, as particle size is the only distinguishing synthesis factor between them.

Consistent with the Table 2, Fig. 8b highlights the dominance of micropores over mesopores. The peak pore diameters within the mesopore and micropore ranges are 3.7 nm and 0.7 nm respectively, for all three samples. No macropores with widths between 50 nm and 100 nm were observed but based on the SEM images we know macropores with diameters between 1 μm to 50 μm are abundantly present in structure of the matrix samples.

3.2. Thermal energy storage analysis

In this section the initial energy storage densities of the activated biochar matrices and composite samples are presented to analyze the effect of particle size on their capacity to store energy. The initial energy storage density here refers to the exothermic heat per unit mass that completely dehydrated samples release during their first hydration cycle, indicating their maximum energy storage density under the applied humidity and temperature. Fig. 9a and Fig. 9b illustrate the initial energy storage density of the activated biochar matrix samples and composite samples, respectively. Supplementary Fig. 1 presents the DSC and TG curves of the first two hydration/dehydration cycles of the composite samples for additional information.

The P-values from the ANOVA are 0.075 and 5×10^{-8} for the matrix and composite samples, respectively. This indicates that particle size does not have a significant effect on the initial energy storage density of the activated biochar samples but has a highly significant effect on the initial energy storage density of the composite samples at the 0.05 alpha level.

While the activated biochar samples exhibit an energy storage density comparable to many low-grade energy storage materials [48,69–73], they do not achieve the impressive energy storage densities observed in the synthesized composite samples. Furthermore, since particle size has no significant effect on the energy storage density of the matrix, an approximate value of 90 J/g can be considered as the average energy storage density for all activated biochar matrix samples.

Fig. 9b shows that sample C1 with smallest particle diameter has the lowest energy storage density. This can be attributed to excessive crushing of the matrix, which leads to the destruction of macropores and poor salt retention. Additionally, as the particle diameter increases from less than 125 μm for sample C1 to between 354 μm and 595 μm for sample C4, the energy storage density increases due to more adequate salt deposition within the porous structure. Further increase in particle diameter leads to a decrease in energy storage density. This is due to excessive salt deposition on the external surface (Fig. 5e and 5f), while the inner pores become less accessible for salt deposition. Thus, an optimal average initial energy storage density of approximately 2480 J/g was achieved by sample C4, which is 66.8 % of the average energy density of the pure $CaCl_2$ reference samples hydrated under the same condition. This indicates that activated biochar particles with diameter between 354 μm and 595 μm provide the highest salt impregnation capacity among the synthesized activated biochar/$CaCl_2$ composite samples. The confidence interval for sample C6 is large because only one or two particles can fit inside the STA pan, resulting in extensive variance. The average salt content of the composite samples, calculated from Eq. (4), follows a similar trend. Samples C1 to C6 are estimated to have an average salt content of 36.9 wt%, 48.6 wt%, 61.3 wt%, 66.8 wt%, 59.1 wt%, and 46.8 wt% of $CaCl_2$ based on their energy storage density. Although the total surface area (S_{tot}, Table 2) has decreased in all composite samples relative to their respective matrices by a similar degree, the salt content varies significantly among the samples with different particle size. This is because the BET surface area and the calculated pore volume derived from nitrogen adsorption/desorption isotherms account only for mesoporous and microporous structures, excluding macropores. As previously discussed, the macropores in composite samples C1 and C2, which have the smallest particle size

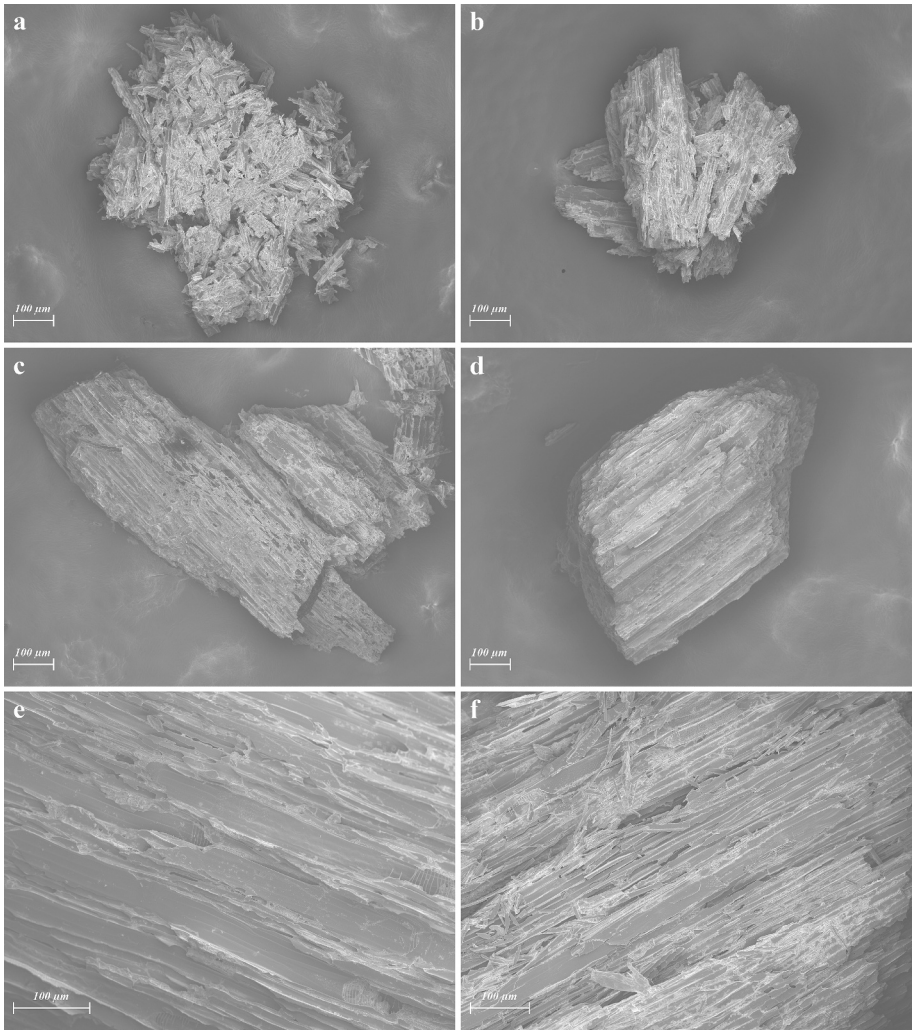

Fig. 7. The SEM image of the (a) composite sample C1, (b) C2, (c) C3, (d) C4, (e) C5, and (f) C6 after 1, 5, 5, 5, 1, and 1 leakage test cycles respectively.

Table 2
The surface area and pore volume of the samples B1, B4, B6, C1, C4, and C6.

Sample	S_{tot}[a] (m^2/g)	S_{meso}[b] (m^2/g)	S_{micro}[c] (m^2/g)	S_{meso}/S_{tot}	V_{tot}[d] (cm^3/g)	V_{meso}[e] (cm^3/g)	V_{micro}[f] (cm^3/g)	V_{meso}/V_{tot}
B1	803	139	664	0.17	0.48	0.17	0.31	0.36
B4	789	133	656	0.17	0.46	0.16	0.30	0.34
B6	765	109	656	0.14	0.41	0.12	0.29	0.29
C1	83	36	46	0.44	0.09	0.06	0.03	0.65
C4	65	28	37	0.43	0.08	0.05	0.02	0.71
C6	64	26	38	0.41	0.08	0.06	0.02	0.73

[a] Total surface area estimated based on BET method.
[b] Mesoporous surface area.
[c] Microporous surface area.
[d] Total volume of the pores.
[e] Mesoporous volume.
[f] Microporous volume.

among the samples, are largely damaged due to excessive crushing. The resulting decrease in their energy storage densities further supports the critical role of macroporous volume in determining both salt storage capacity and overall energy storage performance. Additionally, the pronounced salt agglomeration observed in samples C1 and C2 may reduce salt uptake and promote adhesion of the salt solution to the walls of the sample containers during the soaking stage of the synthesis process.

It is worth noting that the 66.8 wt% is slightly higher than the 65 wt % of salt mixed with the activated biochar. This may be due to imperfect homogeneity of the samples, contributions from the matrix in water vapor absorption, beneficial or even synergic absorption effects that might occur when salt and matrix are mixed. These effects include improved salt dispersion [74], enhanced accessibility and mass transfer of water vapor to salt [75], combined physisorption by matrix and chemisorption by salt [75,76], improved retention of absorbed water [77], and capillary action [27,77].

Table 3 compares sorption-based TCES composites with carbon-

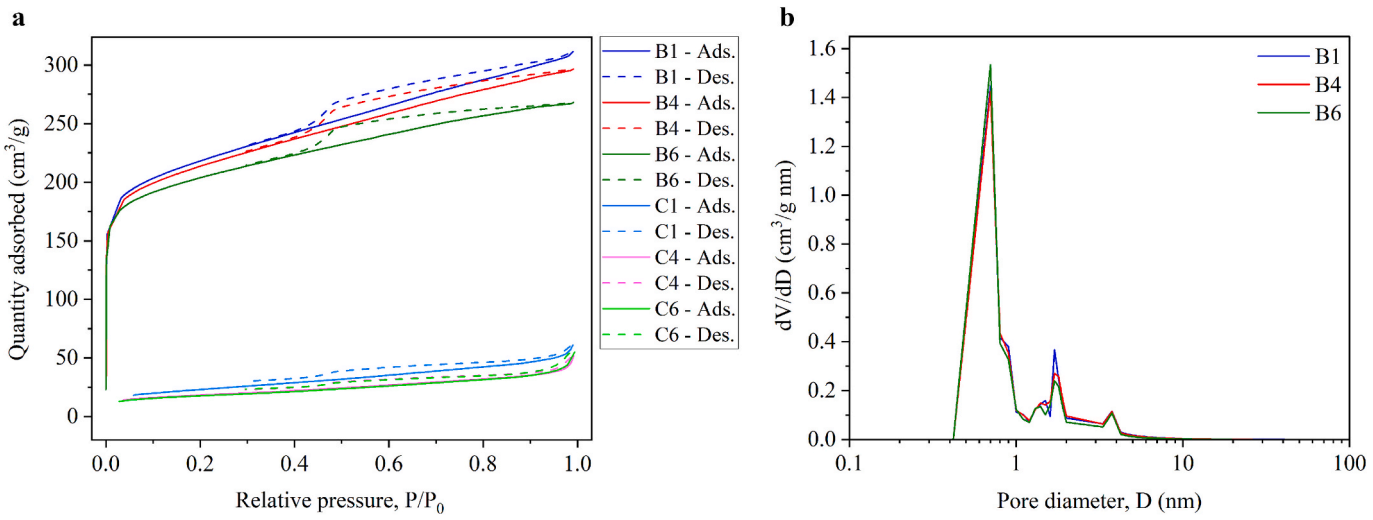

Fig. 8. (a) Nitrogen adsorption/desorption isotherms of samples B1, B4, B6, C1, C4, and C6 and (b) pore size distribution of samples B1, B4, B6 estimated using the BJH and MP methods. 'Ads.' and 'Des.' represent the adsorption and desorption branches of the isotherms, respectively.

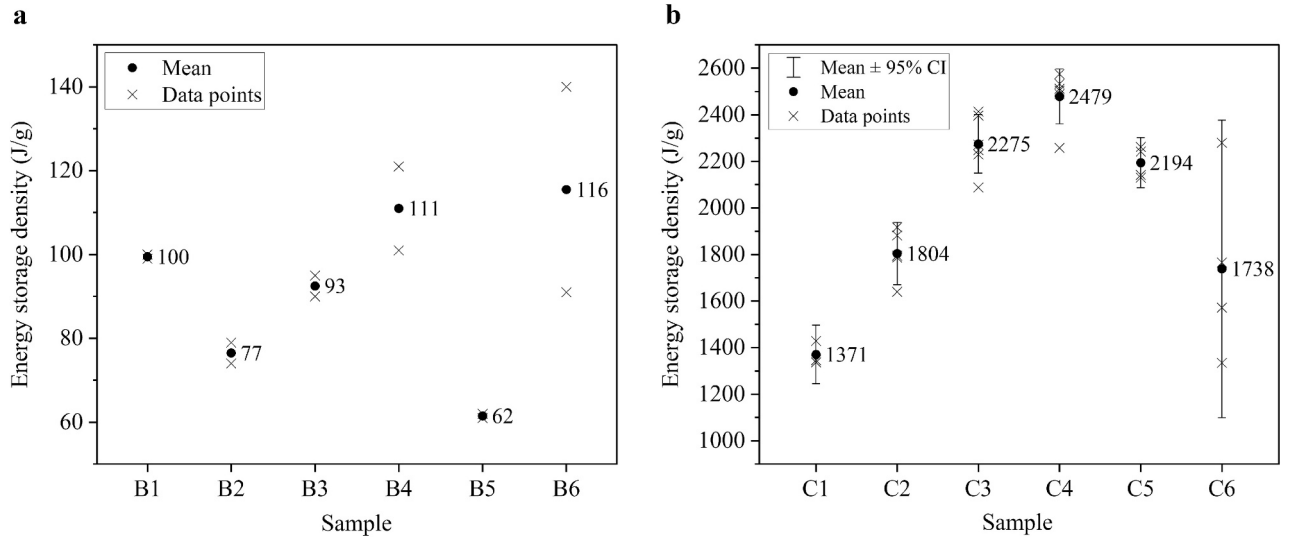

Fig. 9. The initial energy storage density of the activated biochar samples (a) and composite samples (b) including individual data points, mean values and 95 % confidence intervals (shown for composite samples only). The hydration temperature and relative humidity during the hydration step were 35 °C and 35 %, respectively.

based matrices reported in the literature to the TCES composite synthesized in this study. In general, increasing humidity enhances energy storage density; however, supplying humid air with high humidity during winter can be costly. The composites synthesized in this work, particularly sample C4, with a particle size between 354 μm and 595 μm, exhibited higher energy densities than most other carbon-based TCES materials reported in the literature, even at significantly lower relative humidity.

3.3. Cyclic performance analysis

Fig. 10a shows the energy storage density of pure $CaCl_2$ compared to the samples C2, C3, and C4 over 10 consecutive hydration/dehydration cycles. As previously discussed, this method does not consider the salt leakage, and it cannot measure the energy density loss due to leakage. This method is only suitable for assessing the loss of energy density due to degradation of the matrix and/or the active material. The pure $CaCl_2$ sample maintains a stable average energy storage density of approximately 3700 J/g through the cycles. As the energy storage density of the pure $CaCl_2$ remains stable, the slight loss of energy storage density observed in other samples can be attributed to matrix degradation caused by the expansion and contraction of the salt hydrate, as well as the redistribution of salt. This redistribution can block pores, thereby reducing the water uptake capacity while the volume changes of the salt hydrate can further damage the biochar structure.

Fig. 10b exhibits the energy storage density of composite samples in the leakage test. The energy density at cycle 0 represents the average initial energy density of the samples before conducting the leakage test as shown in Fig. 9b. Samples C4, C5, and C6, which have larger particle size, show a significant drop in energy storage density at the first cycle of the leakage test. This is because the salt deposited on their external surface is easily washed away during hydration and subsequently absorbed by the filter paper. The other samples with smaller particle sizes do not exhibit a significant energy density loss in the first cycle, as the agglomerated salt-composite structure (Fig. 5a-c and Fig. 7a-c) prevents the liquefied salt from dripping onto the filter paper. However, with further hydration/dehydration cycles, the agglomerated structure eventually falls apart, leading to salt removal (Fig. 10b, samples C2 and

Table 3
Sorption-based TCES composites with matrices composed of carbon. Particle diameter (d), nominal salt content (SC_N), actual salt content (SC_A), hydration temperature (T_h), dehydration temperature (T_d), initial energy storage density (ESD).

Salt	Matrix		SC_n (wt%)	SC_a (wt%)	T_h (°C)	T_d (°C)	RH (%)	ESD (J/g)	Ref.
$CaCl_2$	Activated carbon	Source: 1	–	13.0	20	200	80	967	[33]
		Source: 2		34.8				2073	
		Source: 3		43.4				2981	
		Source: 4		23.6				2093	
$MgSO_4$	Activated carbon		5	4.1	30	300	30	375	[39]
			10	10.9			30	550	
			20	20.3			30	700	
			30	26.0			30	865	
			30	26.0			60	1325	
			40	35.4			30	915	
$MgSO_4$	Bead-shaped activated carbon		–	1.0	30	150	60	445	[78]
				5.2				642	
				7.6				920	
$MgSO_4$	Expanded graphite		50	56.5	25	150	85	496	[79]
			60	58.9				576	
			70	74.1				632	
			80	87.5				719	
$LiOH{\cdot}H_2O$	Expanded graphite		85	–	30	150	60	680	[80]
			88					810	
			92					1120	
			95					1175	
$CaCl_2$	Expanded graphite		–	23.8	30	200	60	582	[81]
				36.2				1372	
				48.1				1637	
$MgSO_4$	Biochar(derived from corn cob)		5	4.4	30	150	60	360	[74]
			10	9.1				426	
			15	12.6				574	
			20	19.5				635	
LiOH	Activated Biochar(derived from corn cob)		20	–	30	200	80	1421	[82]
			30					1525	
			40					1866	
			50					1672	
$CaCl_2$	Activated Biochar(derived from alder wood)	d < 125 μm	65	36.9	35	120	35	1371	This Work
		125 μm < d < 250 μm		48.6				1804	
		250 μm < d < 354 μm		61.3				2275	
		354 μm < d < 595 μm		66.8				2479	
		595 μm < d < 1600 μm		59.1				2194	
		1600 μm < d		46.8				1738	

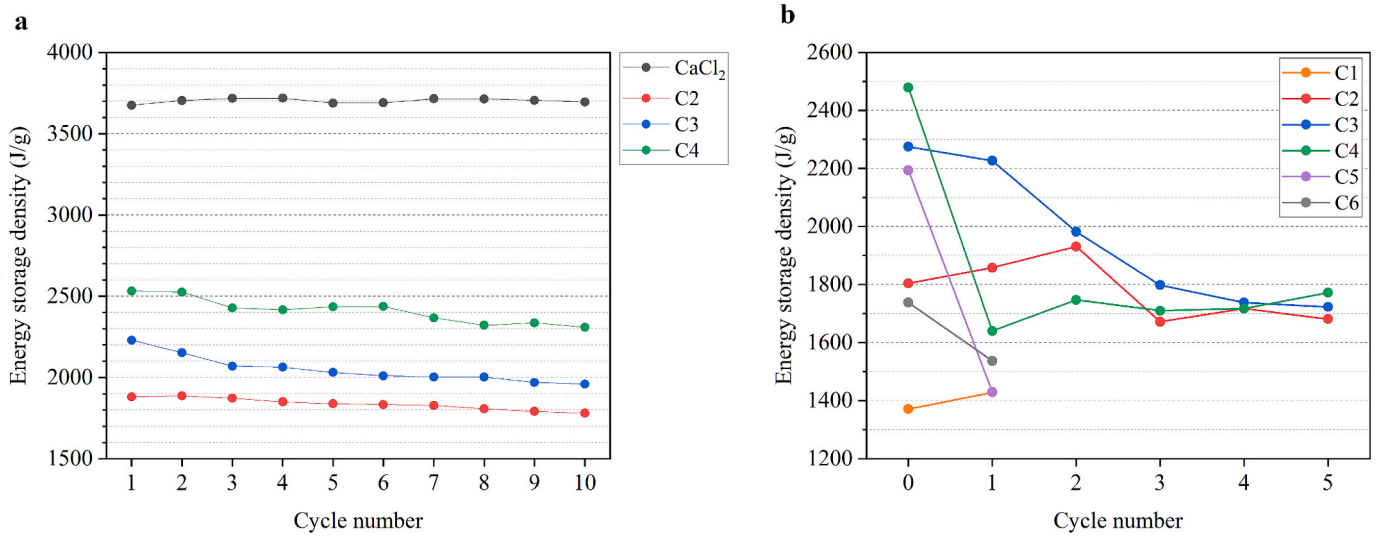

Fig. 10. The energy storage density of pure $CaCl_2$ comparing to samples C2, C3, C4 over ten consecutive hydration/dehydration cycles (a) and the energy storage density of the composite samples over five cycles of our designed leakage test (b). The hydration temperature and relative humidity for both tests were 35 °C and 35 % respectively.

C3). In contrast, sample C4, with a larger particle size compared to samples C2 and C3, retains salt within its inner pores from the second leakage cycle onward, maintaining an impressive energy density of over 1700 J/g, corresponding to 70 % of the initial energy storage density.

By comparing the energy storage density of the C2, C3, and C4 composite samples after five consecutive hydration/dehydration cycles (Fig. 10a) and their energy storage density after five leakage test cycles (Fig. 10b), the necessity of assessing stability of sorption-based TCES materials with a well-designed leakage test rather than continuous cycling with thermal analysis instruments such as DSC, TGA, or STA becomes clear. The energy storage density loss of the composite samples in leakage test is significantly more than consecutive hydration/dehydration measurements. In literature, e.g. in references [30,31,33,39,83,84], the energy storage densities of sorption-based TCES materials are commonly measured with the mentioned thermal analyzers over consecutive hydration/dehydration cycles, which overlooks the significant energy storage density loss due to leakage and confirms what was stated in section 2.2.3. While the research synthesizes a sustainable material for storing thermal energy with outstanding energy density and promising stability, it does not explore the effects of the salt-to-matrix ratio or sorption process parameters, which open doors for further research.

The slight increase in energy storage density observed in some cycles is attributed to sample non-uniformity after each leakage cycle and does not indicate an actual rise in their average energy storage density.

4. Conclusion

This study synthesized a nature-inspired sorption-based thermochemical energy storage composite utilizing sustainable components of activated biochar derived from wood biomass as the porous matrix and $CaCl_2$ as the sorbent salt. The activated biochar synthesized in this research exhibited a hierarchical multiscale porous structure with an impressive surface area of approximately 800 m^2/g. We utilized a simple yet effective salt impregnation method to incorporate 65 wt% $CaCl_2$ into the porous matrix, harnessing the natural vascular architecture of the wood. Additionally, we explored the impact of particle size on the energy storage density and cyclability of the composite. The leakage test method introduced in this study provides accurate quantitative data based on energy storage density, in contrast to the qualitative visual leakage observations commonly reported in the literature. This was supported by the fact that energy storage density loss of the composite samples in the leakage test was significantly more than the consecutive hydration/dehydration of the samples in the STA. The $CaCl_2$/activated biochar composite sample with a particle diameter between 354 μm and 595 μm exhibited optimal performance, achieving a remarkable average initial energy storage density of approximately 2480 J/g, which remained stable at 2310 J/g after 10 consecutive hydration/dehydration in STA. This sample also achieved the highest energy storage density of approximately 1780 J/g after 5 cycles of the designed leakage test.

Successful impregnation of the $CaCl_2$ into the inner pores of the activated biochar in the sample with a particle diameter between 354 μm and 595 μm was confirmed by X-ray micro-computed tomography. SEM images revealed intense agglomeration of the composite particles with diameters smaller than 250 μm and excessive salt deposition on the outer surfaces of particles with diameters larger than 595 μm leading to relatively inferior performance. EDS maps of the surface of the composite clarify that the salt prefers to deposit along surface grooves of the activated biochar matrix, i.e. tracheids and vessels, due to stronger capillary action in these areas.

The $CaCl_2$/activated biochar composite synthesized in this study offers long-term thermal energy storage with minimal losses, making it highly promising for applications like space heating. In addition to the mentioned factors, future studies should also evaluate the material in a large-scale setup to achieve a satisfactory balance between material-level performance and system-level efficiency.

CRediT authorship contribution statement

Ali Kasebi Vayghan: Writing – original draft, Visualization, Validation, Software, Methodology, Investigation, Formal analysis, Data curation, Conceptualization. **Maryam Roza Yazdani McCord:** Writing – review & editing, Validation, Supervision, Resources, Methodology, Investigation, Funding acquisition, Conceptualization. **Annukka Santasalo-Aarnio:** Writing – review & editing, Validation, Supervision. **Ari Seppälä:** Writing – review & editing, Validation, Supervision, Resources, Project administration, Funding acquisition, Conceptualization.

Declaration of competing interest

The authors declare the following financial interests/personal relationships which may be considered as potential competing interests: Ari Seppala reports financial support was provided by Research Council of Finland. Maryam Yazdani McCord reports financial support was provided by Research Council of Finland. Ari Seppala reports financial support was provided by Finnish Cultural Foundation. If there are other authors, they declare that they have no known competing financial interests or personal relationships that could have appeared to influence the work reported in this paper.

Acknowledgements

This project has received funding from the European Union – NextGenerationEU instrument and is funded by the Research Council of Finland under grant number 353297. This research is also funded by Research Council of Finland (No. 343192, SoMa Project). In addition, the work is supported by Finnish Cultural Foundation grant no. 00231064. We would also like to thank Dr. Heikki Suhonen from Helsinki University for performing the micro-CT scans.

Appendix A. Supplementary material

Supplementary data to this article can be found online at https://doi.org/10.1016/j.enconman.2025.120532.

Data availability

Data will be made available on request.

References

[1] Ang T-Z, Salem M, Kamarol M, Das HS, Nazari MA, Prabaharan N. A comprehensive study of renewable energy sources: Classifications, challenges and suggestions. Energ Strat Rev 2022;43:100939.
[2] Mahon H, O'Connor D, Friedrich D, Hughes B. A review of thermal energy storage technologies for seasonal loops. Energy 2022;239:122207.
[3] Miró L, Gasia J, Cabeza LF. Thermal energy storage (TES) for industrial waste heat (IWH) recovery: a review. Appl Energy 2016;179:284–301.
[4] Koohi-Fayegh S, Rosen MA. A review of energy storage types, applications and recent developments. J Storage Mater 2020;27:101047.
[5] Chen X, Zhang D, Wang Y, Ling X, Jin X. The role of sensible heat in a concentrated solar power plant with thermochemical energy storage. Energ Conver Manage 2019;190:42–53.
[6] Palomba V, Frazzica A. Comparative analysis of thermal energy storage technologies through the definition of suitable key performance indicators. Energ Buildings 2019;185:88–102.
[7] Zhou X, Xu Y, Zhang X, Xu D, Linghu Y, Guo H, et al. Large scale underground seasonal thermal energy storage in China. J Storage Mater 2021;33:102026.
[8] Bauer T, Odenthal C, Bonk A. Molten salt storage for power generation. Chem Ing Tech 2021;93(4):534–46.
[9] Li B, Ju F, Xiao M, Ning P. Mechanical stability of granite as thermal energy storage material: an experimental investigation. Eng Fract Mech 2019;211:61–9.
[10] Jouhara H, Żabnieńska-Góra A, Khordehgah N, Ahmad D, Lipinski T. Latent thermal energy storage technologies and applications: a review. Int J Therm 2020;5:100039.
[11] Opolot M, Zhao C, Liu M, Mancin S, Bruno F, Hooman K. A review of high temperature (≥ 500° C) latent heat thermal energy storage. Renew Sustain Energy Rev 2022;160:112293.

[12] Aftab W, Usman A, Shi J, Yuan K, Qin M, Zou R. Phase change material-integrated latent heat storage systems for sustainable energy solutions. Energ Environ Sci 2021;14(8):4268–91.
[13] Desai F, Prasad JS, Muthukumar P, Rahman MM. Thermochemical energy storage system for cooling and process heating applications: a review. Energ Conver Manage 2021;229:113617.
[14] Aydin D, Casey SP, Riffat S. The latest advancements on thermochemical heat storage systems. Renew Sustain Energy Rev 2015;41:356–67.
[15] Sadeghi G. Energy storage on demand: thermal energy storage development, materials, design, and integration challenges. Energy Storage Mater 2022;46:192–222.
[16] Yan T, Zhang H. A critical review of salt hydrates as thermochemical sorption heat storage materials: thermophysical properties and reaction kinetics. Sol Energy 2022;242:157–83.
[17] Padamurthy A, Nandanavanam J, Rajagopalan P. Assessment of selected salt hydrates for thermochemical energy storage applications. Mater Today Proc 2022;64:1609–15.
[18] Spietz T, Fryza R, Lasek J, Zuwała J. Thermochemical energy storage based on salt hydrates: a comprehensive review. Energies 2025;18(10):2643.
[19] Stitou D, Goetz V, Spinner B. A new analytical model for solid-gas thermochemical reactors based on thermophysical properties of the reactive medium. Chem Eng Process 1997;36(1):29–43.
[20] Yang H, Wang C, Tong L, Yin S, Wang L, Ding Y. Salt hydrate adsorption material-based thermochemical energy storage for space heating application: a review. Energies 2023;16(6):2875.
[21] Frazzica A, Brancato V, Caprì A, Cannilla C, Gordeeva L, Aristov Y. Development of "salt in porous matrix" composites based on LiCl for sorption thermal energy storage. Energy 2020;208:118338.
[22] Steinhauser G. Cleaner production in the Solvay process: general strategies and recent developments. J Clean Prod 2008;16(7):833–41.
[23] Ozankaya G. Experimental Investigations of Thermochemical Heat Storage System Using Hydrated Salt Based Composite Sorbents for Building Space Heating Applications. Eastern Mediterranean University (EMU)-Doğu Akdeniz Üniversitesi (DAÜ); 2018.
[24] Zhang Y, Wang R. Sorption thermal energy storage: concept, process, applications and perspectives. Energy Storage Mater 2020;27:352–69.
[25] Gaeini M, Rouws A, Salari J, Zondag H, Rindt C. Characterization of microencapsulated and impregnated porous host materials based on calcium chloride for thermochemical energy storage. Appl Energy 2018;212:1165–77.
[26] Mehrabadi A, Farid M. New salt hydrate composite for low-grade thermal energy storage. Energy 2018;164:194–203.
[27] Wang J, Wang R, Wang L. Water vapor sorption performance of ACF-$CaCl_2$ and silica gel-$CaCl_2$ composite adsorbents. Appl Therm Eng 2016;100:893–901.
[28] Korhammer K, Druske M-M, Fopah-Lele A, Rammelberg HU, Wegscheider N, Opel O, et al. Sorption and thermal characterization of composite materials based on chlorides for thermal energy storage. Appl Energy 2016;162:1462–72.
[29] Touloumet Q, Silvester L, Bois L, Postole G, Auroux A. Water sorption and heat storage in $CaCl_2$ impregnated aluminium fumarate MOFs. Sol Energy Mater Sol Cells 2021;231:111332.
[30] Barsk A, Yazdani MR, Kankkunen A, Seppälä A. Exceptionally high energy storage density for seasonal thermochemical energy storage by encapsulation of calcium chloride into hydrophobic nanosilica capsules. Sol Energy Mater Sol Cells 2023;251:112154.
[31] Shkatulov A, Joosten R, Fischer H, Huinink H. Core–shell encapsulation of salt hydrates into mesoporous silica shells for thermochemical energy storage. ACS Appl Energy Mater 2020;3(7):6860–9.
[32] Palacios A, Navarro ME, Barreneche C, Ding Y. Water sorption-based thermochemical storage materials: a review from material candidates to manufacturing routes. Front Therm Eng 2022;2:1003863.
[33] Zhang Q, Wu Y, Dong S, Zhuo J, Sun X, Yao Q. Development of activated carbon/$CaCl_2$ composites for seasonal thermochemical energy storage: effect of pore structure. J Storage Mater 2024;97:112697.
[34] McCord MRY, Seppälä A, Kasmaei MP, Zimmerman JB, Rojas OJ. From low conductivity to high energy efficiency: the role of conductive polymers in phase change materials. Chem Eng J 2025:160804.
[35] Nonnen T, Preißler H, Kött S, Beckert S, Gläser R. Salt inclusion and deliquescence in salt/zeolite X composites for thermochemical heat storage. Microporous Mesoporous Mater 2020;303:110239.
[36] Li W, Klemeš JJ, Wang Q, Zeng M. Characterisation and sorption behaviour of LiOH-LiCl@ EG composite sorbents for thermochemical energy storage with controllable thermal upgradeability. Chem Eng J 2021;421:129586.
[37] Ding B, Xu C, Liao Z, Ye F. Study on long-term thermochemical thermal storage performance based on $SrBr_2$-expanded vermiculite composite materials. J Storage Mater 2021;42:103081.
[38] Ousaleh HA, Said S, Zaki A, Faik A, El Bouari A. Silica gel/inorganic salts composites for thermochemical heat storage: improvement of energy storage density and assessment of cycling stability. Mater Today Proc 2020;30:937–41.
[39] Bennici S, Dutournié P, Cathalan J, Zbair M, Nguyen MH, Scuiller E, et al. Heat storage: hydration investigation of $MgSO_4$/active carbon composites, from material development to domestic applications scenarios. Renew Sustain Energy Rev 2022;158:112197.
[40] Lee HW, Kim Y-M, Kim S, Ryu C, Park SH, Park Y-K. Review of the use of activated biochar for energy and environmental applications. Carbon Lett. 2018;26:1–10.
[41] Yazdani MR, Duimovich N, Tiraferri A, Laurell P, Borghei M, Zimmerman JB, et al. Tailored mesoporous biochar sorbents from pinecone biomass for the adsorption of natural organic matter from lake water. J Mol Liq 2019;291:111248.
[42] Zhou M, Wang J, Zhao Y, Wang G, Gu W, Ji G. Hierarchically porous wood-derived carbon scaffold embedded phase change materials for integrated thermal energy management, electromagnetic interference shielding and multifunctional application. Carbon 2021;183:515–24.
[43] Zhang Y, Wang R, Li T. Thermochemical characterizations of high-stable activated alumina/LiCl composites with multistage sorption process for thermal storage. Energy 2018;156:240–9.
[44] Gordeeva L, Aristov YI. Composites 'salt inside porous matrix'for adsorption heat transformation: a current state-of-the-art and new trends. Int J Low-Carbon Technol 2012;7(4):288–302.
[45] Wan Y-C, Chen Y, Cui Z-X, Ding H, Gao S-F, Han Z, et al. A promising form-stable phase change material prepared using cost effective pinecone biochar as the matrix of palmitic acid for thermal energy storage. Sci Rep 2019;9(1):11535.
[46] Mandal S, Ishak S, Adnin RJ, Lee D-E, Park T. An approach to utilize date seeds biochar as waste material for thermal energy storage applications. J Storage Mater 2023;68:107739.
[47] Xie N, Luo J, Li Z, Huang Z, Gao X, Fang Y, et al. Salt hydrate/expanded vermiculite composite as a form-stable phase change material for building energy storage. Sol Energy Mater Sol Cells 2019;189:33–42.
[48] Atinafu DG, Wi S, Yun BY, Kim S. Engineering biochar with multiwalled carbon nanotube for efficient phase change material encapsulation and thermal energy storage. Energy 2021;216:119294.
[49] Wei Z, Zhang Y, Cai C, Qu H, Fu Y, Tan SC. Wood lamella-inspired photothermal stearic acid-eutectic gallium-indium-based phase change aerogel for thermal management and infrared stealth. Small 2023;19(46):2302886.
[50] Courbon E, D'Ans P, Permyakova A, Skrylnyk O, Steunou N, Degrez M, et al. Further improvement of the synthesis of silica gel and $CaCl_2$ composites: enhancement of energy storage density and stability over cycles for solar heat storage coupled with space heating applications. Sol Energy 2017;157:532–41.
[51] Shkatulov A, Houben J, Fischer H, Huinink H. Stabilization of K_2CO_3 in vermiculite for thermochemical energy storage. Renew Energy 2020;150:990–1000.
[52] Tomin O, Vahala R, Yazdani MR. Synthesis and efficiency comparison of reed straw-based biochar as a mesoporous adsorbent for ionic dyes removal. Heliyon 2024;10(2).
[53] Rasa K, Viherä-Aarnio A, Rytkönen P, Hyväluoma J, Kaseva J, Suhonen H, et al. Quantitative analysis of feedstock structural properties can help to produce willow biochar with homogenous pore system. Ind Crop Prod 2021;166:113475.
[54] Hyväluoma J, Kulju S, Hannula M, Wikberg H, Källi A, Rasa K. Quantitative characterization of pore structure of several biochars with 3D imaging. Environ Sci Pollut Res 2018;25:25648–58.
[55] Brunauer S, Emmett PH, Teller E. Adsorption of gases in multimolecular layers. J Am Chem Soc 1938;60(2):309–19.
[56] Barrett EP, Joyner LG, Halenda PP. The determination of pore volume and area distributions in porous substances. I. Computations from nitrogen isotherms. J Am Chem Soc 1951;73(1):373–80.
[57] Mikhail RS, Brunauer S, Bodor E. Investigations of a complete pore structure analysis: I. Analysis of micropores. J Colloid Interface Sci 1968;26(1):45–53.
[58] Sing KS. Reporting physisorption data for gas/solid systems with special reference to the determination of surface area and porosity (Recommendations 1984). Pure Appl Chem 1985;57(4):603–19.
[59] Zbair M, Bennici S. Survey summary on salts hydrates and composites used in thermochemical sorption heat storage: a review. Energies 2021;14(11):3105.
[60] Berglund LA, Burgert I. Bioinspired wood nanotechnology for functional materials. Adv Mater 2018;30(19):1704285.
[61] Chen C, Kuang Y, Zhu S, Burgert I, Keplinger T, Gong A, et al. Structure–property–function relationships of natural and engineered wood. Nat Rev Mater 2020;5(9):642–66.
[62] Gholizadeh M, Meca S, Zhang S, Clarens F, Hu X. Understanding the dependence of biochar properties on different types of biomass. Waste Manag 2024;182:142–63.
[63] Leng L, Xiong Q, Yang L, Li H, Zhou Y, Zhang W, et al. An overview on engineering the surface area and porosity of biochar. Sci Total Environ 2021;763:144204.
[64] Lechman J, Lu N. Capillary force and water retention between two uneven-sized particles. J Eng Mech 2008;134(5):374–84.
[65] McCulfor J, Himes P, Anklam MR. The effects of capillary forces on the flow properties of glass particle suspensions in mineral oil. AIChE J 2011;57(9):2334–40.
[66] Pham ST, Chareyre B, Tsotsas E, Kharaghani A. Pore network modeling of phase distribution and capillary force evolution during slow drying of particle aggregates. Powder Technol 2022;407:117627.
[67] Kärger J, Valiullin R. Mass transfer in mesoporous materials: the benefit of microscopic diffusion measurement. Chem Soc Rev 2013;42(9):4172–97.
[68] Thommes M, Kaneko K, Neimark AV, Olivier JP, Rodriguez-Reinoso F, Rouquerol J, et al. Physisorption of gases, with special reference to the evaluation of surface area and pore size distribution (IUPAC Technical Report). Pure Appl Chem 2015;87(9–10):1051–69.
[69] Zhou Y, Wang X, Liu X, Sheng D, Ji F, Dong L, et al. Multifunctional ZnO/polyurethane-based solid-solid phase change materials with graphene aerogel. Sol Energy Mater Sol Cells 2019;193:13–21.
[70] Gu X, Liu P, Liu C, Peng L, He H. A novel form-stable phase change material of palmitic acid-carbonized pepper straw for thermal energy storage. Mater Lett 2019;248:12–5.
[71] Lu X, Liu H, Murugadoss V, Seok I, Huang J, Ryu JE, et al. Polyethylene glycol/carbon black shape-stable phase change composites for peak load regulating of electric power system and corresponding thermal energy storage. Eng Sci 2020;9(24):25–34.

[72] Zuo X, Li J, Zhao X, Yang H, Chen D. Emerging paraffin/carbon-coated nanoscroll composite phase change material for thermal energy storage. Renew Energy 2020; 152:579–89.
[73] Chakraborty A, Ahmed S, Shamberger P, Yu C. Achieving extraordinary thermal stability of salt hydrate eutectic composites by amending crystallization behaviour with thickener. Compos B Eng 2023;264:110877.
[74] Nguyen MH, Zbair M, Dutournié P, Limousy L, Bennici S. Corn cobs' biochar as green host of salt hydrates for enhancing the water sorption kinetics in thermochemical heat storage systems. Molecules 2023;28(14):5381.
[75] An H, Chen Y, Wang Y, Liu X, Ren Y, Kang Z, et al. High-performance solar-driven water harvesting from air with a cheap and scalable hygroscopic salt modified metal–organic framework. Chem Eng J 2023;461:141955.
[76] Permyakova A, Wang S, Courbon E, Nouar F, Heymans N, d'Ans P, et al. Design of salt–metal organic framework composites for seasonal heat storage applications. J Mater Chem A 2017;5(25):12889–98.
[77] Lee X, Yang F, Xing Y, Huang Y, Xu L, Liu Z, et al. Use of biochar to manage soil salts and water: effects and mechanisms. Catena 2022;211:106018.
[78] Nguyen MH, Zbair M, Dutournié P, Bennici S. Thermochemical sorption heat storage: investigate the heat released from activated carbon beads used as porous host matrix for MgSO4 salt. J Storage Mater 2023;59:106452.
[79] Miao Q, Zhang Y, Jia X, Li Z, Tan L, Ding Y. $MgSO_4$-expanded graphite composites for mass and heat transfer enhancement of thermochemical energy storage. Sol Energy 2021;220:432–9.
[80] Li W, Klemeš JJ, Wang Q, Zeng M. Development and characteristics analysis of salt-hydrate based composite sorbent for low-grade thermochemical energy storage. Renew Energy 2020;157:920–40.
[81] Gao N, Deng L, Li J, Huang H, Zhou B, Zhou Y. Multi-form heat storage performance of expanded graphite based $CaCl_2$ composites for low-grade heat source. Energy Rep 2022;8:12117–25.
[82] Yang X, Li S, Zhao J, Wang X, Huang H, Wang Y. Construction of biomass waste derived hierarchical porous biochar framework based lithium hydroxide composites for highly efficient and durable low temperature thermochemical heat storage. J Clean Prod 2022;359:132047.
[83] Ristić A, Maučec D, Henninger SK, Kaučič V. New two-component water sorbent CaCl2-FeKIL2 for solar thermal energy storage. Microporous Mesoporous Mater 2012;164:266–72.
[84] Wang Y, Zhang Z, Liu S, Wang Z, Shen Y. Development and characteristics analysis of novel hydrated salt composite adsorbents for thermochemical energy storage. Energies 2023;16(18):6572.